fortune Journals

Research Article

JOURNAL OF SPINE RESEARCH AND SURGERY

ISSN: 2687-8046



Predicting Postoperative Spinal Load Redistribution Following Single- And Dual-Level Lumbar Fusion: An In-Silico Analysis

Farid Amirouche, PhD[1,2], Shreya Kurup, BS[3], Harish Rajavel, MS[2]

Abstract

Purpose: While lumbar fusion provides stability to the affected segment, it also reallocates mechanical load to adjacent unfused regions, contributing to adjacent segment degeneration (ASD). The biomechanical consequences of fusion construct length and location are not well-characterized. This study evaluated the effects of single- and dual-level lateral lumbar interbody fusion constructs on spinal stress distribution at adjacent endplates and intervertebral discs using a validated finite-element model.

Methods: A validated CT-based in silico lumbar spine model (L1-L5) was used to simulate single- and dual-level LLIF constructs under three loading modes. Patient-specific bone material properties were derived from CT imaging. Fusion models incorporating interbody cages with posterior screw-rod fixation were subjected to physiologic flexion, lateral bending, and axial rotation. Stress distribution within adjacent intervertebral discs and vertebral endplates was then quantified.

Results: This model was validated against the range of motion of published cadaveric data under flexion and extension, lateral bending, and axial rotation. Single-level fusion moderately restricted motion at the fused segments, while dual-level fusions significantly decreased flexion and lateral bending by over 60%. The location of the fusion determined adjacent segment motion and stiffness. Single-level fusions elevated adjacent-level stresses by 50% compared to the healthy model. Dual-level fusion exhibited a three-to-four-fold increase in adjacent segment endplate and disc stress, with pronounced stress localization at the outer annulus.

Conclusion: Both single- and dual-level constructs can greatly increase the mechanical demand on adjacent discs and endplates, and this effect scales with construct length. These findings provide biomechanical insight into ASD development.

Keywords: Lumbar fusion; Adjacent segment disease; In silico modeling; von Mises stress; Endplate stress; Intervertebral disc

Introduction

Lumbar spinal fusion is widely performed to treat degenerative disc disease, instability, and deformity [70-74]. However, lumbar fusion is associated with a substantial reoperation burden. In a prospective cohort of 433 patients, Irmola et al. reported a reoperation rate of 19.3% at four years, driven by acute complications such as instrumentation failure and pseudarthrosis [123]. The most common indication for reoperation was adjacent segment degeneration (ASD), which accounted for 8.7% of cases at four years [123]. While spinal

Affiliation:

[1]Department of Orthopaedic Surgery, Northshore University Health System, an Affiliate of the University of Chicago Pritzker School of Medicine. Skokie, Illinois, USA

[2]Department of Orthopaedic Surgery, University of Illinois at Chicago, Chicago, Illinois, USA.

[3]University of Illinois College of Medicine, Chicago, IL, USA.

***Corresponding author:**
Farid Amirouche, PhD, Vice-Chairman, Basic Science Research Orthopaedic and Spine Institute, Department of Orthopaedic Surgery, Endeavor Health (formerly Northshore University HealthSystem), An affiliate of the University of Chicago, Pritzker School of Medicine, 9669 Kenton Avenue Skokie. IL 60076, USA.

Citation: Amirouche F, Kurup S, Rajavel H. Predicting postoperative spinal load redistribution following single- and dual-level lumbar fusion: an in-silico analysis. Journal of Spine Research and Surgery. 8 (2026): 82-100.

Received: November 03, 2026
Accepted: November 10, 2026
Published: November 25, 2026

Amirouche F, et al., J Spine Res Surg 2026
DOI:10.26502/fjsrs00104

fusion eliminates motion at a target segment, providing pain relief and stability, it fundamentally alters the mechanical environment of the adjacent intervertebral discs and facet joints [75,76]. During everyday loading, such as when the spine undergoes flexion, extension, and torsion, the fused segment can no longer absorb or distribute force, so the levels immediately above and below bear greater shear loads and passive moments [77]. Over time, this additional mechanical burden can accelerate the degeneration of the adjacent nucleus pulposus, leading to desiccation and the loss of load-bearing capacity [78,79]. Greater stress is then transferred to the adjacent annulus fibrosus and endplates, eventually causing irreversible changes such as disc height loss, microfractures, and osteophyte formation [78,80,81]. These changes accumulate silently on imaging before eventually manifesting as pain and neurological symptoms, a condition known as adjacent segment disease [84-87]. Adjacent segment disease is one of the most common indications for revision surgery after lumbar fusion, typically emerging around five to seven years postoperatively [75,85,88-91]. A meta-analysis of over 34,000 patients found that radiographic ASD occurred in nearly 30% of lumbar fusion patients, with symptoms present in around 8.5%, and that this rate increased with longer follow-up, so understanding who is most at risk and why is essential for anticipating and reducing ASD risk [124].

The likelihood of developing ASD is based on a combination of patient-specific and surgical factors. Characteristics such as obesity, osteoporosis, and advanced age can accelerate ASD [92,93]. Patients who have physically demanding occupations requiring repetitive bending, lifting, or prolonged sitting may be at higher risk for developing ASD as well [94]. Fusion has been found to increase the range of motion and stress at the upper adjacent level post-fixation, potentially contributing to ASD [125]. The extent of the spinal fusion also plays a role in the long-term viability of the adjacent segments [95,96]. Multilevel constructs restrict mobility more broadly than single-level fusion, forcing greater compensatory load onto the remaining unfused segments [97]. The literature has reported conflicting findings regarding the relationship between construct length and ASD risk. Sears et al. found that patients with three or four levels fused were three times more likely to develop ASD compared to those with a single-level fusion, and those with a dual-level fusion were twice as likely [96]. Another study confirmed this finding, reporting that multilevel fusion increased the likelihood of ASD compared to single-level fusion. Conversely, Ghiselli et al. found that patients with multilevel fusion had significantly less adjacent segment disease than those with single-level fusion. This inconsistency highlights how much remains unknown about the mechanical consequences of the extent of fusion.

Despite growing awareness of these risk factors, preventing ASD remains an unsolved clinical problem. Motion-preserving surgeries have been developed as an alternative, but evidence for their efficacy remains inconclusive [98-100]. A key limitation in studying ASD is that the spine's internal mechanical environment cannot be directly observed. Stress redistribution and altered motion at adjacent segments are invisible on MRI and CT and only become apparent once structural damage has already occurred. To study ASD, research approaches have included cadaveric testing, imaging-based assessments, and computational modeling [101,102]. Cadaveric studies can measure motion and load transfer, but they are constrained by tissue availability, ethical considerations, and an inability to replicate patient-specific variables such as bone density or long-term degenerative progression [103,104]. Computational simulation addresses these limitations by modeling the spine as it exists in a specific patient, accounting for bone geometry, material properties, and anatomical relationships that cadaveric or imaging studies cannot fully capture [126]. While imaging characterizes structural changes that have already occurred, computational simulations can quantify stress to identify mechanical environments that may predispose adjacent tissues to subsequent degeneration. These models can reveal the mechanical environment that may drive degeneration before it becomes visible, which can allow surgeons to anticipate which segments are most at risk, refine implant selection, and make more informed preoperative decisions.

Computational modeling has enabled researchers to study spinal fusion under controlled conditions that would be impossible to replicate clinically, by varying fusion levels, implant strategies, and loading configurations while measuring the mechanical response [105,106]. These models can be derived directly from patient CT data, producing anatomically representative simulations that reflect individual bone geometry and material properties [108,109]. This allows researchers to estimate how a specific spinal geometry may respond to different surgical constructs before the incision is made. Developing these simulations directly benefits our understanding of fusion biomechanics. For example, models have been used to demonstrate how even a single-level fusion can elevate motion and intradiscal pressure at neighboring segments [112,113], and extending the fusion to additional levels further increases ligament and annular stress at both the superior and inferior adjacent levels [114]. Findings that highlight these changes in stress concentrations, pressure changes, and altered range of motion cannot be measured intraoperatively or seen in postoperative imaging; however, the strong agreement between CT-based computational models and cadaveric measurements confirms that these predictions are not just theoretical [110, 111].

Lateral lumbar interbody fusion (LLIF) is a minimally invasive approach that restores disc height and decompresses the spine through a lateral corridor and has become

increasingly used for degenerative disease and ASD [115,116]. Like other fusion techniques, LLIF redistributes mechanical load to adjacent segments, but the extent of this redistribution depends heavily on patient-specific anatomy [117]. Studies accounting for individual bone density, disc quality, and vertebral geometry have shown that adjacent-level mechanics can vary dramatically between patients, meaning that generalizations about how fusion affects the spine may not hold for any given individual [119]. Prior patient-specific computational work has demonstrated that patient-specific factors can lead to heterogeneous changes in adjacent-disc degeneration and vertebral bone remodeling, which supports the importance of incorporating a patient's specific anatomy and tissue characteristics into biomechanical assessment [127].

This is where CT-based computational modeling offers a meaningful clinical advantage. By deriving material properties directly from CT imaging, the model captures spinal heterogeneity that uniform models miss, which include cortical bone thickness, trabecular architecture, and abnormalities such as sclerotic endplates and osteoporotic regions [120,121,122]. This offers several advantages. First, it allows quantification of global and local stress distributions in adjacent discs and endplates relative to a healthy baseline. Second, in patients with compromised bone quality, it can help us visualize the unique spatial distribution of stress, especially at bone-implant or bone-disc junctions. Finally, simulations allow us to test hypothetical surgical scenarios by varying cage placement, bone stiffness, or fusion extent that cannot be tested safely or practically in vivo. Building on prior cadaveric investigations of multilevel LLIF constructs [28,29], this study uses a patient-specific CT-based computational model to predict how single- and dual-level fusion configurations alter stress distribution and mechanical demand at adjacent discs and endplates, thereby better informing construct selection and surgical planning. Additionally, this model uses three loading modes—flexion, lateral bending, and torsion—which could be extended to future analyses of occupational vibration exposure (e.g., long-haul driving) and interbody cage durability, applications that have less commonly been explored in prior ASD finite element studies.

Methods

Biomechanical study design

A subject-specific finite element model of the lumbar spine from L1 to L5 was developed to evaluate how single- and dual-level LLIF constructs alter mechanical demand at adjacent endplates and intervertebral discs. Stress distribution at adjacent segments was quantified to characterize postoperative load redistribution and identify regions of elevated mechanical demand. Intersegmental range of motion was evaluated only for the intact configuration and used exclusively to validate the model against experimental data and confirm the physiological accuracy of the finite element formulation. After validation, all comparative assessments were based on stress responses in healthy, single-level fusion, and dual-level fusion configurations under flexion, lateral bending, and torsion loading, to isolate how construct length and fusion level influence stress amplification at non-fused segments.

Finite element model generation

The finite element model was developed using full-size CT scan data encompassing the cervical through lumbar spine. The CT image stack was imported into Mimics (Materialise, Plymouth, MI, USA), and the lumbar region was isolated by cropping the dataset using multiplanar reconstructions in the sagittal and coronal views. This process enabled accurate identification of vertebral geometry and surface features, ensuring that native spinal curvature, vertebral alignment, and intervertebral disc spacing were preserved as represented in the original scan. Since the geometry was derived directly from the CT data, no additional translational or rotational realignment of the vertebrae was required during model construction (Figures 1a and 1b). Following segmentation, the geometries were transferred to SpaceClaim (ANSYS Inc., Canonsburg, PA, USA), where intervertebral discs, LLIF cages, and ligamentous structures were manually generated according to the spatial relationships defined by the adjacent vertebral bodies (Figure 1b).

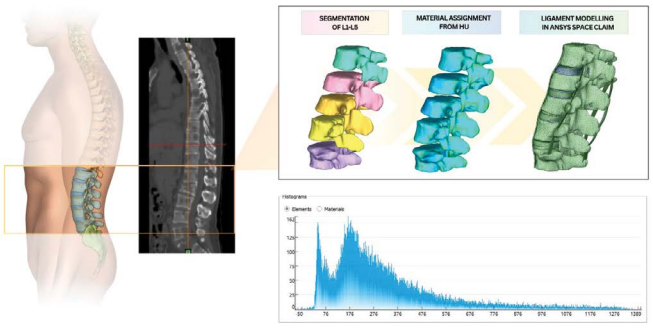


Figure 1: Sagittal view of CT scans (a), Process flow of CAD model development and meshing (b), Element count at each voxel intensity (c)

Material assignment and ligament modeling

Heterogeneous material properties were assigned throughout the vertebral bone based on CT-derived density distributions to account for spatial variations in stiffness across cortical and cancellous regions. These regions were represented using grayscale intensity to capture the distributions of density and Young's modulus from the CT dataset. Grayscale intensity was quantified using Hounsfield units (HU) and then converted as a function of density, which was subsequently used to define Young's modulus

Amirouche F, et al., J Spine Res Surg 2026
DOI:10.26502/fjsrs00104

through established density to Young's modulus relationships [42]. The resulting modulus values ranged from 235 to 1019 MPa and were derived directly from the grayscale intensity distribution in the CT dataset. While many studies assign idealized isotropic properties for cortical bone, often up to 12,000 MPa, to represent a thoroughly segmented cortical shell, the current approach assigns effective elastic properties based on spatially resolved density within the scanned specimen. Cortical bone is thin and located at the outer boundary of the vertebral geometry, so partial-volume averaging during CT imaging can reduce apparent HU in these peripheral regions. Although this may underrepresent the peak modulus of isolated cortical structures, the approach preserves specimen-specific heterogeneity (Figure 2) and avoids abrupt stiffness transitions between material zones. The Poisson ratio for different vertebral sections is constant at 0.3, as it is a function of deformation, and we assume that the vertebrae deform uniformly [42]. Each vertebra is assigned a material bin of 35 (Figure 2), which is automatically distributed throughout the cortical and trabecular regions to capture the spatial heterogeneity in stiffness.

A larger number of material bins can be used to refine further the density and modulus distributions derived from CT grayscale values, but this also increases computational cost due to more material definitions and associated element-level calculations. To justify the selected discretization, a sensitivity comparison was performed between models using 50 and 35 material bins, and the resulting stress and deformation responses showed no meaningful differences in standard deviation for this patient-specific dataset. Since increasing the number of bins did not produce a significant change in the mechanical response while substantially increasing computational expense, 35 material bins were selected as an optimal balance between numerical efficiency and accurate representation of spatial stiffness variation. This

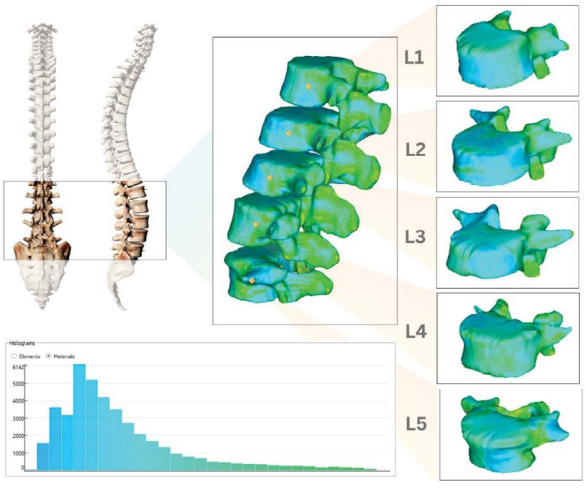


Figure 2: Element count distribution by assigned Young's modulus and spatial mapping of Young's modulus across the vertebrae.

methodology can accurately represent physiologic variations in bone density and provides a realistic response to subsequent simulations.

The vertebral geometries and material segmentation were generated directly in Mimics (Materialise, Plymouth, MI, USA), where CT-based density mapping and material bin assignment were applied at the element level. The volumetric mesh was generated directly from the segmented CT geometry in Mimics/3-matic (Materialise, Plymouth, MI, USA) with no further geometric modifications. It was exported as a pre-meshed model with element-wise material properties to ANYSYS Workbench. Since geometry, mesh, and material assignment were generated together, the mesh was not regenerated or refined within ANSYS prior to analysis. By doing this, the CT-derived material distribution was preserved exactly when imported into the Workbench environment, without remeshing or reassignment of material properties. For further model development, the intervertebral discs, lateral lumbar interbody fusion (LLIF) cages, and ligamentous structures were manually reconstructed in SpaceClaim (ANSYS Inc., Canonsburg, PA, USA) based on the anatomical geometry and spatial constraints of the individual vertebrae. The vertebral endplate thickness was modeled at $0.8 \pm (0.1–0.2$ mm), consistent with the upper range reported by Hou et al [33]. This reconstruction strategy was adopted to ensure anatomically accurate disc height and ligament geometry, which directly influence load transfer and local stress distribution across the endplate-disc interface.

The posterior and anterior longitudinal elements (Figure 3a) were constructed and attached based on geometric continuity and standard anatomical landmarks. The intervertebral disc was modeled with four layers of the annulus fibrosus (Figure 3). The annulus ground substance, which represents the thin layer on the outer surface of the intervertebral disc, is effectively modeled as a surface-coating feature in Ansys Workbench (ANSYS Inc., Canonsburg, PA, USA). The coating function in ANSYS allows a thin layer of material to be applied over the surface of an existing solid body without requiring a separate body or solid mesh [44,45]. It is typically used to model layered structures or surface-bound materials with defined thicknesses and material properties, while maintaining simple meshes. Modeling the annulus as multiple layers with a surface coating representation enables realistic anisotropic stress transmission under bending and torsional loading. Preserving physiologic endplate thickness and disc structure improves the prediction of localized stress concentrations, which are critical for assessing the mechanical demand of the adjacent segment and potential damage patterns.

The annulus was segmented into distinct regions to better represent its anisotropic mechanical behavior. At the same time, the nucleus pulposus was assumed to share a similar

Amirouche F, et al., J Spine Res Surg 2026
DOI:10.26502/fjsrs00104

profile with the annulus following the approach of Cappetti et al [43]. The nucleus pulposus was constructed with four concentric lamellar layers representing the annulus fibrosus, based on standard anatomical organization. The remaining central volume within the disc boundary, enclosed by the inner annular layer, was assigned as the nucleus pulposus.

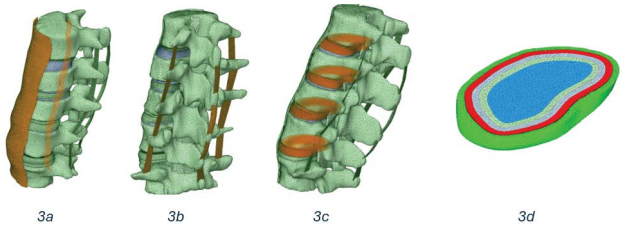


Figure 3: Soft tissue setup showing the intervertebral discs and ligaments integrated with the vertebral mesh: (a) intertransverse ligament, (b) anterior longitudinal ligament, (c) posterior longitudinal ligament, and (d) annulus fibrosus.

Major ligament groups, including the anterior longitudinal, posterior longitudinal, and intertransverse ligaments, were modeled using hyperelastic material properties suitable for large non-linear deformations (Figure 3b). Ligament mechanics were formulated using Green-Lagrange strain and second Piola-Kirchhoff stress measures, consistent with the finite strain analysis of soft biological tissues [44,45]. Including these ligaments demonstrates the model's thoroughness, reassuring spine biomechanics researchers and surgeons of its biomechanical relevance. In most prior studies, the intertransverse ligament was modeled with one-dimensional spring elements to achieve computational efficiency and leverage its simple geometry [56]. Although efficient, this approach may not capture the full three-dimensional geometry and spatial deformation behavior of the ligament. Therefore, in the present study, the intertransverse ligament was modeled as a three-dimensional band extending between adjacent transverse processes, from the inferior edge of the superior transverse process to the superior edge of the inferior transverse process. The thickness of the intertransverse ligament was set at 1.0 mm (± 0.2 mm), in agreement with morphological descriptions.

Modeling of lumbar interbody implants and posterior fixation

A NuVasive CoRoent XL-XW polyetheretherketone (PEEK) interbody cage with an anteroposterior width of 26 mm was used. Single-level fusion models involved cage placement at individual intervertebral levels (L1-L2, L2-L3, L3-L4, and L4-L5), while the remaining levels were left intact. In dual-level fusion models, cages were incorporated across two contiguous levels to simulate extended fusion constructs while leaving the remaining stages intact. These models enabled a direct comparison of the effects of increasing fusion construct length on stress redistribution at adjacent vertebral endplates and intervertebral discs. For each configuration, implant height in the superior-inferior direction and length in the medial-lateral direction were determined directly from CT measurements and adjusted as required to maintain anatomical conformity and appropriate disc space restoration.

The positioning of the pedicle screw was verified through pedicle fit analysis at each level (Figure 4), confirming sufficient margins and safe trajectories, with no cortical breach that could lead to nerve damage. Clearence also represents the safety margin typically achieved with image-guided navigation. The 5 mm diameter was selected based on prior finite element findings by Qi et al [46], which showed that increasing screw diameter from 4.0 mm to 6.5 mm reduces stress concentrations in cortical and cancellous bone while limiting axial pull displacement. Screws with a diameter less than 5 mm have been reported to provide an optimal balance between reducing local stress & maintaining stability, supporting the use of screws in the 5- 6.5 mm range for lumbar fixations.

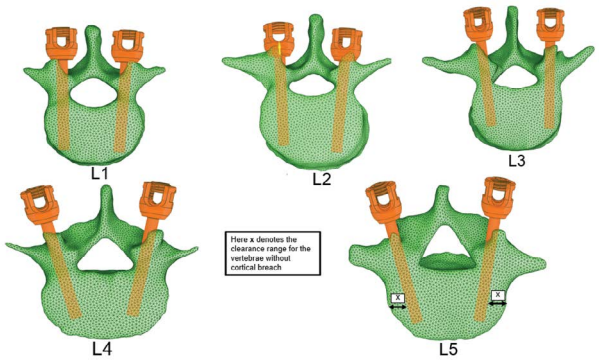


Figure 4: Pedicle screws fit analysis

The choice of a 26 mm cage was made to maximize endplate coverage, particularly over the apophyseal ring, which represents the strongest region of the vertebral body. Wider cages distribute axial loads over a larger contact area, thereby reducing localized stress and the risk of subsidence. Prior biomechanical investigations have demonstrated that cages of this dimension provide superior segmental stability and reduce subsidence compared to narrower implants (18-22 mm in diameter) [24-27]. During cage insertion, only the cartilaginous endplate was removed while preserving the subchondral bony endplate, consistent with clinical practice [47]. Removal of the cartilage exposes vascularized bone, promoting osseous integration and enhancing the implant's mechanical grip, whereas retaining it would inhibit fusion and increase the risk of subsidence. This also directly influences contact mechanics and stress transfer at the cage endplate interface. This step was reflected in the segmentation process, as the grayscale threshold used in Mimics (-1024 to 1650 HU) excluded low-density cartilage, resulting in vertebral models composed only of cortical and trabecular bone. However, during cage insertion, the cartilaginous endplate was removed

Amirouche F, et al., J Spine Res Surg 2026
DOI:10.26502/fjsrs00104

as part of the surgical procedure. A thin, compliant layer was retained at the implant interface to account for possible remnants of cartilage or transitional tissue that may remain following curettage. This layer was not directly visible in the CT dataset since it lies below the grayscale threshold used in Mimics. Still, it was incorporated into the model with an elastic modulus of 24 MPa based on previously reported values for the cartilaginous endplate. Although the vertebral endplate geometry primarily represents the subchondral bony surface, incorporating this thin, compliant layer allowed the model to better capture early postoperative contact mechanics at the cage-endplate interface and better represent the mechanical transition between the implant and underlying bone.

Bone graft modeling within the interbody cage

Bone graft material was placed within the central cavity of the LLIF cage to simulate standard clinical practice, where osteoconductive fillers are used to promote interbody fusion. In the model, this region was defined as a separate volume within the implant and assigned a material property representative of post-healing conditions. Specifically, a homogeneous elastic modulus of 100 MPa was applied (Table 1), reflecting the mechanical behavior of a partially consolidated bone graft, which is like that of the cancellous bone section and consistent with prior studies modeling post-fusion states [56]. This representation captures the filler material's load-sharing contribution while maintaining continuity with the cage structure under simulated loading. Incorporating the graft material allows stress to be partially transferred through the cage core rather than being concentrated solely at the cage endplate interface, which is critical for evaluating realistic stress magnitudes and identifying damage-prone regions in adjacent segments under physiological loading.

Finite element model validation and boundary conditions

To analyze stress-related outcomes and potential damage patterns, the finite element model must first be validated to confirm that it is numerically and mechanically representative of the physical system. To do this, we developed the healthy and fully fused spine FE model, comparing its responses with in vitro testing of a cadaveric sample using intersegmental range of motion metrics, such as flexion-extension, lateral bending, and axial rotation. Since displacement is the primary solution variable in finite element analysis, and all strain and stress quantities are derived from it, agreement in the range of motion indicates that the geometry, material assignment, and boundary conditions are correctly defined. With this validated baseline, stress-strain and contact-pressure results obtained in single- and dual-level fusion configurations can be attributed to construct-induced effects rather than numerical inaccuracies.

The finite element model was constrained at the inferior endplate of L5, corresponding to the experimental fixation of S1 in a metallic pot. A simplified base support was introduced using multipoint constraint (MPC) beam elements applied only to the central region of the L5 endplate to allow some mobility and provide a moment arm equal to the distance from S1 to L5. This also prevents the artificial stiffening that occurs with one-dimensional beam elements when rigid connections are distributed across the entire endplate surface, thereby preserving physiologic compliance during bending and torsion.

The spinal model was meshed with linear tetrahedral elements, which reproduced segmental range of motion more accurately than quadratic elements and reduced node count by about 65%. Quadratic tetrahedral elements consistently underestimated motion, potentially due to the sensitivity of midside nodes to boundaries and implant contacts, leading to localized over-constraint. Linear elements, therefore, provide computational efficiency by reducing the number of interpolation points in the model while maintaining physiological kinematics. By effectively reducing the node count while having the same elements, the obtained mesh was optimal and consistent with all three configurations, as loading was applied at the superior end of L1. The model was preloaded in accordance with the experimental configuration (Figure 6) used by Mok et al., in which eccentric compression induced bending. The resulting deformed configuration from this preload step was imported into a separate static structural module, where pure moments were applied. This approach ensures that the flexion-extension, lateral bending, and axial rotation simulations reflect the post-compression state of the construct, capturing the combined effect of axial and bending loads consistent with in vitro testing conditions. Pure moments of 6 Nm were applied for flexion-extension and lateral bending, and axial rotation was modeled using an 8-degree

Table 1: Summary of material and element properties used for the FE model.

Part	Reference	Young's modulus	Poisson ratio
Vertebral end plate	Zhang et al.[48]	24	0.4
Annulus fibrosus - Ground substance	Goel et al.[49]	2	0.45
Intervertebral cage (isotropic)	Zhang et al.[48]	3600	0.3
Bone graft	Akamaru et al.[50]	100	0.2
Pedicle screws (Titanium alloy)	Qi et al.[46]	110000	0.3
Connecting rods (Titanium alloy)	Qi et al.[46]	110000	0.3

Amirouche F, et al., J Spine Res Surg 2026
DOI:10.26502/fjsrs00104

rotation about the Z-axis. The moment magnitude of 6 Nm was selected based on the lower bound of the experimental range reported in Mok et al., where applied flexion and extension moments varied between 4.5 and 6 Nm. Previous in vitro studies have typically used pure moments of 6-8 Nm for lumbar spine biomechanics; however, since the present model was developed for validation against the specific experimental configuration reported by Mok et al., the lower limit of their applied range was adopted. Additionally, in the current setup, the S1 vertebra was not explicitly modeled and was instead represented by beam elements at the L5 base (Figure 5). The beam length (60mm) was set to match the distance covered by the S1 segment's height and the fixture setup used in the experiment. This simplification increases construct stiffness and may underestimate segmental motion. Hence, selecting the lower moment value ensured that the model response remained conservative and within the physiologic range observed in comparable experimental studies. This represents the exact loading condition in the references, as the MTS machine provides axial rotation via displacement, which is easier to control and calibrate. Also, the preliminary output of these studies is stiffness, which is a measure of resistance to displacement. Hence, maintaining the axial rotation is much more effective. These load cases matched the experimental testing protocol and allowed monitoring of intersegmental motion across the different constructs [28,29]. The axial rotation was applied about the global Z-axis, which was aligned along the superior-inferior direction of the lumbar spine. This axis was maintained consistently across all configurations, including the intact and instrumented models. Since the anatomical orientation of the spine was preserved throughout model development and all loading was applied in reference to this orientation, the applied rotation direction remained physiologically representative and comparable across constructs.

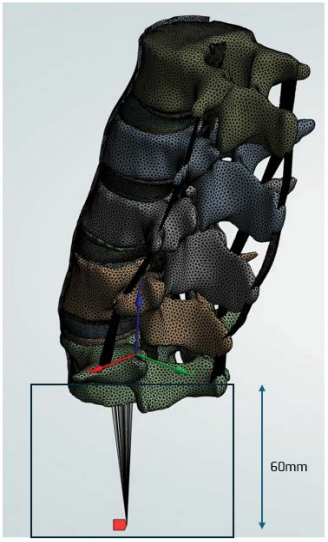


Figure 5: MPC constraint using beam elements

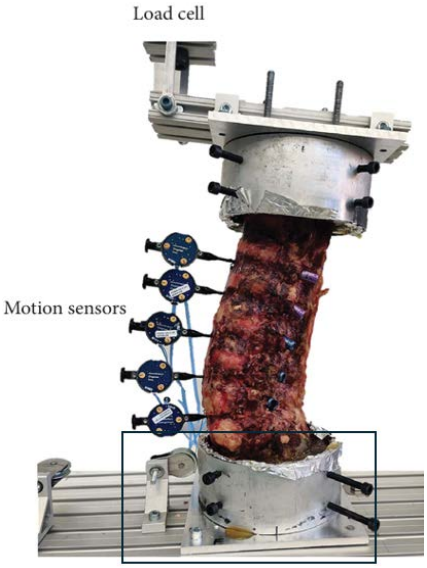


Figure 6: Experimental setup

For the healthy lumbar and fully fused models, intersegmental motion was first quantified using range of motion measurements to establish a baseline for numerical validation. Range of motion was sampled at approximately 15 nodes distributed over anatomically representative regions, and the resulting motion was averaged to characterize segmental kinematics. Using multiple nodes rather than a single point reduces sensitivity to local mesh effects. It provides a more stable representation of overall segment behavior that can be directly compared with experimental measurements. Once an acceptable agreement with experimental range of motion data was achieved, the model was considered mechanically representative and suitable for stress-based evaluation.

Stress evaluation

Following baseline validation, stress was evaluated at the vertebral endplates and intervertebral discs, as these regions are primary load-transfer interfaces and are clinically associated with subsidence and adjacent-segment degeneration. Von Mises stress was selected because it represents the combined effect of compressive shear and bending stresses that occur simultaneously in spinal tissues under physiological loading. Endplates were examined because they directly transmit load between the vertebral body and the interbody space and are susceptible to localized overload following fusion. Intervertebral discs were evaluated because altered motion and load redistribution after fusion can elevate internal disc stress at adjacent levels, providing insight into potential mechanisms of degeneration. Since vertebral geometry was derived from segmented CT data, sharp corners inherent to the reconstructed region can produce stress singularities, where computed stress rises as a function of mesh density rather than truly representing a stress value. To reduce their influence on reported results, stress values were averaged

Amirouche F, et al., J Spine Res Surg 2026
DOI:10.26502/fjsrs00104

across regions of interest rather than isolated peak nodes to better reflect the regional mechanical demand relevant to tissue-level damage.

Results

Model validation (Healthy)

The intact lumbar spine model developed in this study was validated by comparing its segmental range of motion with previously published experimental data. The computed range of motion values for flexion (Figure 7a), lateral bending (Figure 7b), and axial rotation (Figure 7c) were within range of previous experiments [28]. In each loading condition, several values fell within the standard deviation range of the experimental data, confirming the accuracy of the finite element simulation. The model reproduced expected trends across all loading modes, including progressive reductions in motion at lower lumbar levels and preservation of physiologic motion patterns (Figure 8). Based on this agreement, the model was considered validated and appropriate for evaluating how fusion constructs alter mechanical demand at adjacent segments.

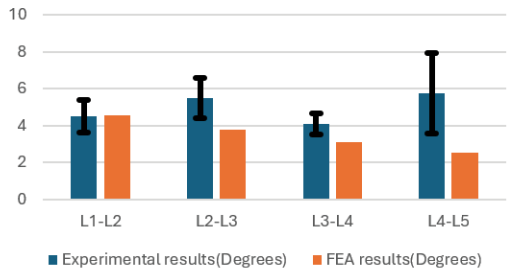


Figure 7a: Comparison of healthy FE model to experimental values in flexion loading.

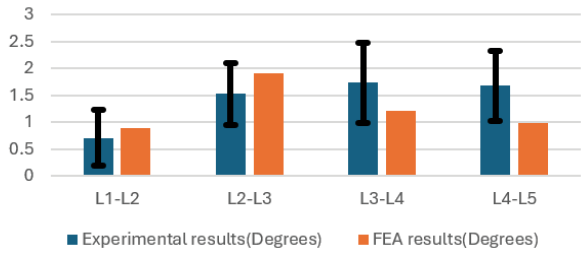


Figure 7b: Comparison of healthy FE model to experimental values in torsional loading.

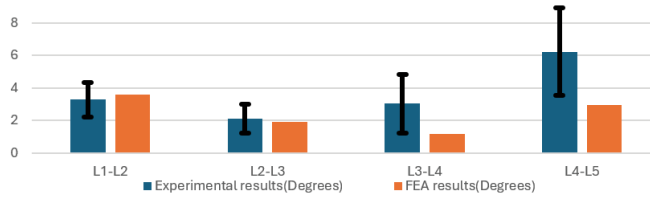


Figure 7c: Comparison of healthy FE model to experimental values in lateral loading.

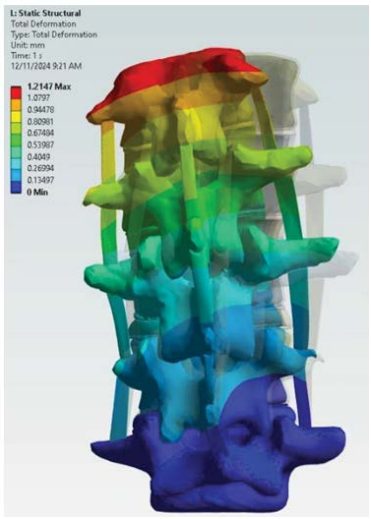


Figure 8: Finite element result for healthy lumbar spine model.

Model validation (Fully fused)

The inclusion of fully fused configurations was necessary to establish a mechanically constrained reference state in which motion is minimized by cage placement, bone graft material, and posterior fixation, allowing verification of implant positioning, graft load sharing, and construct-level behavior independent of ligament-driven kinematics observed in the healthy model.

Like the healthy model validation, the fully fused lumbar spine configurations were assessed by examining their segmental range of motion responses to flexion, extension, lateral bending, and axial rotation relative to the intact baseline model. The computed range of motion values for the multilevel fusion constructs showed marked suppression of motion at the instrumented levels across all loading modes, as illustrated in Figure 9. In flexion-extension, the fused segments exhibited pronounced reductions in motion with corresponding redistribution at adjacent levels. At the same time, lateral bending and axial rotation demonstrated near elimination of motion at the fused levels (Figure 10). The suppression of motion at instrumented levels across all loading modes confirms that the construct behaves as expected following fusion, giving confidence that stress-based comparisons between single- and dual-level fusion configurations reflect true construct-induced effects.

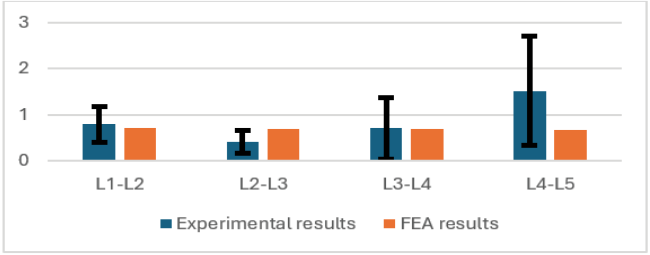


Figure 9a: Comparison of multilevel fused FE model to experimental values in flexion loading.

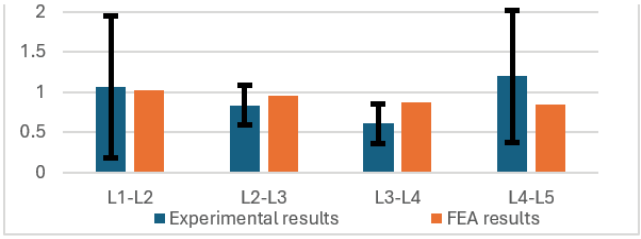


Figure 9b: Comparison of the multilevel fused FE model to experimental values in lateral loading.

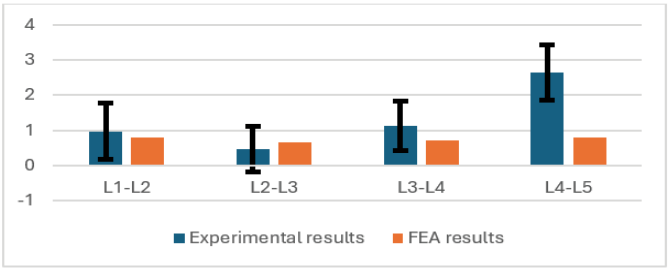


Figure 9c: Comparison of the multilevel fused FE model to experimental values in torsional loading.

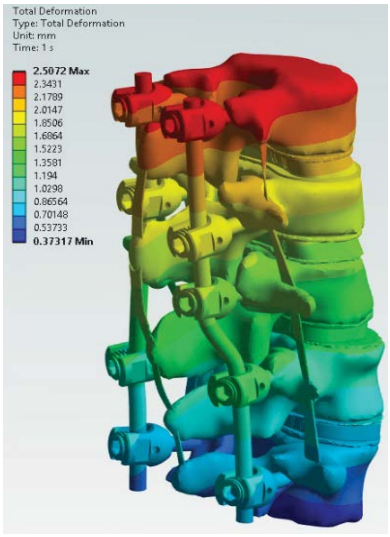


Figure 10: Finite element result for multilevel fused lumbar spine model.

Stress evaluation across fusion configurations

Healthy lumbar configuration

In the healthy lumbar model, stress was evaluated at the vertebral endplates and intervertebral discs to establish a baseline load-sharing pattern before fusion. Endplate stress increased progressively in the caudal direction across all loading modes, with lower lumbar levels exhibiting higher stresses than upper levels. Under flexion, endplate stress increased steadily from L1 to L5, which is consistent with their role in transmitting larger bending moments. A similar caudal increase was observed under lateral bending and torsion, indicating a stable and physiologic stress gradient along the lumbar column (Figure 11). The stress value ranges also correspond well with the existing studies [33]. For each vertebral level, the reported endplate stress represents the average of the superior and inferior endplates at that level (Table 2a,2b,2c). This averaging approach was adopted to provide a single representative stress value per motion segment since adjacent endplates act together in load transmission and are evaluated as a combined mechanical unit when comparing stress across configurations.

Table 2a: Von Mises stress at end plates during flexion loading.

Level	Endplate Evaluated	Stress (MPa)	Avg Stress (Mpa)
L1	L1 lower endplate	0.42	**0.42**
L2	L2 upper endplate	0.55	**0.64**
	L2 lower endplate	0.72	
L3	L3 upper endplate	0.88	**0.99**
	L3 lower endplate	1.1	
L4	L4 upper endplate	1.27	**1.4**

Table 2b: Von Mises stress at end plates during lateral loading.

Level	Endplate Evaluated	Stress (MPa)	Avg stress (Mpa)
L1	L1 lower endplate	0.35	**0.35**
L2	L2 upper endplate	0.45	**0.52**
	L2 lower endplate	0.58	
L3	L3 upper endplate	0.69	**0.75**
	L3 lower endplate	0.81	
L4	L4 upper endplate	0.96	**1.02**
	L4 lower endplate	1.08	

Table 2c: Von Mises stress at end plates during torsional loading.

Level	Endplate Evaluated	Stress (MPa)	Avg stress (Mpa)
L1	L1 lower endplate	0.31	**0.31**
L2	L2 upper endplate	0.39	**0.43**
	L2 lower endplate	0.47	
L3	L3 upper endplate	0.54	**0.59**
	L3 lower endplate	0.63	
L4	L4 upper endplate	0.71	**0.77**
	L4 lower endplate	0.83	

Intervertebral disc stress increased from the upper to lower lumbar spine, with L4 -L5 exhibiting approximately a 95 % higher stress compared to L1- L2 across different loading modes, reflecting the greater mechanical demand carried by the caudal segments under physiological conditions (Table 3). A level-dependent relationship was observed, where cranial levels exhibited greater range of motion and more localized average stress concentrations to the anterior of the disc and endplate, while caudal levels with less motion showed more evenly distributed stress patterns (Figures 11 and 12).

Amirouche F, et al., J Spine Res Surg 2026
DOI:10.26502/fjsrs00104

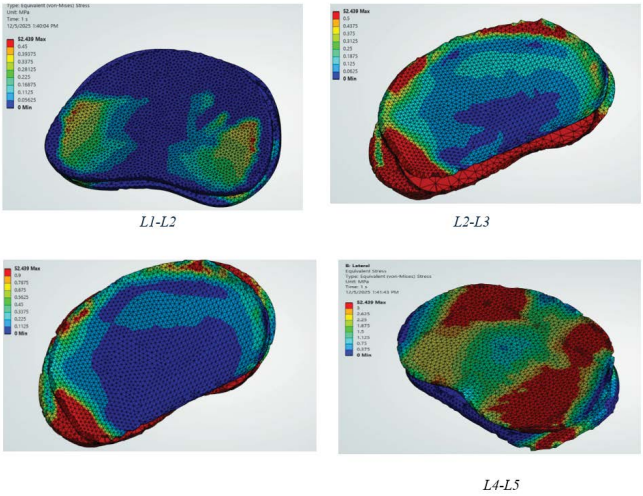


Figure 11: Von Mises stress at end plates under flexion (L1-L5 level)

Table 3: Von Mises stress at the intervertebral disc during loading.

Level	Flexion (MPa)	Lateral Bending (MPa)	Torsion (MPa)
L1-L2	0.39	0.33	0.29
L2-L3	0.51	0.44	0.37
L3-L4	0.64	0.56	0.47
L4-L5	0.76	0.68	0.58

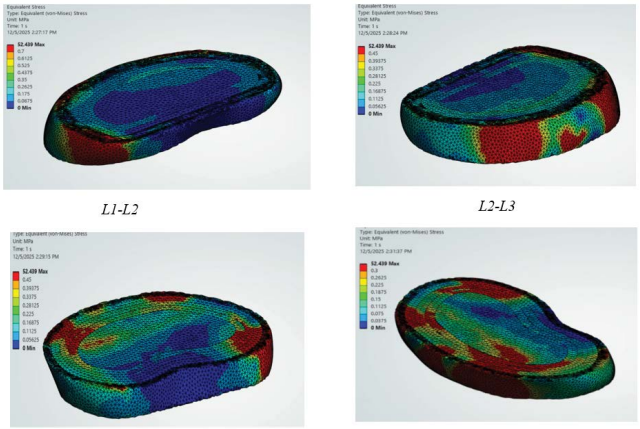


Figure 12: Von Mises stress at intervertebral disc (L1-L5 level).

Single-level fusion configuration

Single-level fusion produced measurable increases in mechanical demand at adjacent endplates and discs across all loading conditions (Table 4). Endplate stress in neighboring segments increased relative to the healthy baseline, with the magnitude of the increase depending on the fusion level. Single-level fusion cases such as L3 - L4 and L4 - L5 resulted in greater stress elevation at adjacent endplates compared to more cranial fusions, reflecting the higher mechanical demand carried by lower lumbar segments. Overall, adjacent-level endplate stress increased by roughly 1.5 to 2 times the healthy condition, depending on the loading mode.

Disc stress adjacent to single-level fusion levels also increased compared to the intact spine. Unlike in the healthy model, where stress was more evenly distributed, disc stress in single-level fusion cases tended to migrate toward the outer annulus, particularly under flexion and lateral bending. This shift indicates increased bending and shear demand at the annular periphery as motion is constrained at the fused segment and transferred to the neighboring disc. These findings suggest that even single-level fusion is sufficient to disrupt normal load sharing and introduce localized stress concentrations in neighboring segments, with direct implications for long-term degeneration risk (Table 5).

Table 4: Von Mises stress at end plates during multiple loading conditions (Single-level fusion).

Fusion Level	Endplate Evaluated	Flexion (MPa)	Lateral Bending (MPa)	Torsion (MPa)
L1-L2	L2 endplates	1	0.76	0.63
L2-L3	L1 end plates	1.12	0.82	0.7
	L3 end plates	1.26	0.96	0.81
L3-L4	L2 endplates	1.32	1	0.85
	L4 endplates	1.48	1.12	0.94
L4-L5	L3 endplates	1.65	1.28	1.1

Table 5: Von Mises stress at intervertebral disc during multiple loading conditions (Single-level fusion).

Fusion Level	Adjacent Healthy Disc	Flexion (MPa)	Lateral Bending (MPa)	Torsion (MPa)
L1-L2	L2 L3	0.6	0.51	0.43
L2-L3	L1 L2	0.44	0.37	0.32
	L3 L4	0.79	0.68	0.57
L3-L4	L2 L3	0.66	0.57	0.48
	L4 L5	1.02	0.9	0.76
L4-L5	L3 L4	0.91	0.79	0.67

Dual-level fusion configuration

Dual-level fusion configurations resulted in the most pronounced stress amplification at adjacent endplates and discs across all loading modes (Table 6). The substantial increase in stress, particularly at the lower lumbar levels, underscores the critical need for careful surgical planning and further investigation to prevent overload-related complications.

Table 6: Von Mises stress at end plates during multiple loading conditions (Dual-level fusion).

Fusion level	Adjacency	Endplate Evaluated	Flexion (MPa)	Lateral (MPa)	Torsion (MPa)
L1–L3 fused	Second-Level Adjacent	L3-L4	2.15	1.72	1.29
	Immediate Adjacent	L4-L5	2.78	2.14	1.65
L3–L5 fused	Second-Level Adjacent	L1-L2	3.1	2.41	1.86
	Immediate Adjacent	L2-L3	3.62	2.98	2.2

Table 7: Von Mises stress at the intervertebral disc during multiple loading conditions (Dual-level fusion).

Fusion level	Adjacency	Adjacent Level	Flexion (MPa)	Lateral Bending (MPa)	Torsion (MPa)
L1–L3 fused	Immediate Adjacent	L3-L4	2.32	2.01	1.72
	Second-Level Adjacent	L4-L5	2.87	2.42	2.03
L3–L5 fused	Second-Level Adjacent	L1-L2	2.19	1.84	1.56
	Immediate Adjacent	L2-L3	2.68	2.29	1.95

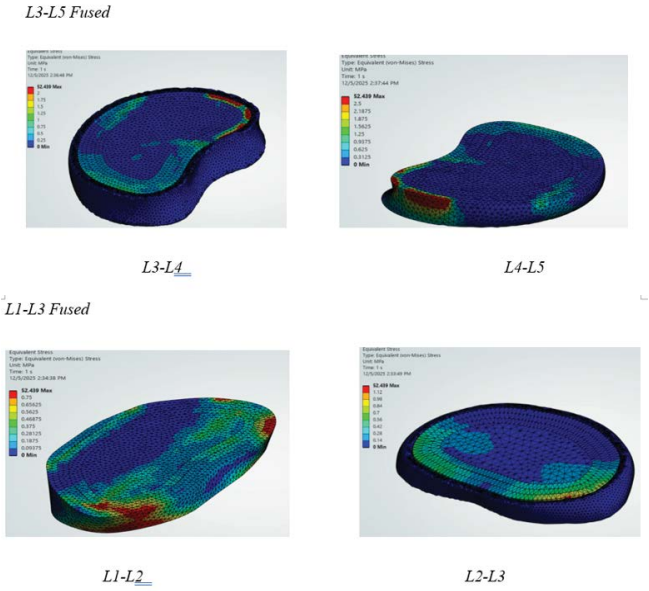


Figure 13: Von Mises stress at the intervertebral disc for dual-level fusion under flexion (L1-L5 level).

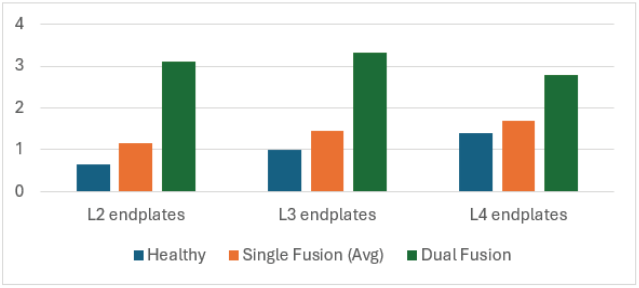


Figure 14a: Von Mises stress comparison at end plates for flexion.

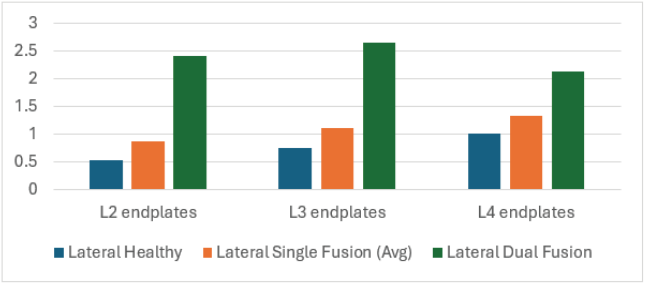


Figure 14b: Von Mises stress comparison at end plates for lateral bending.

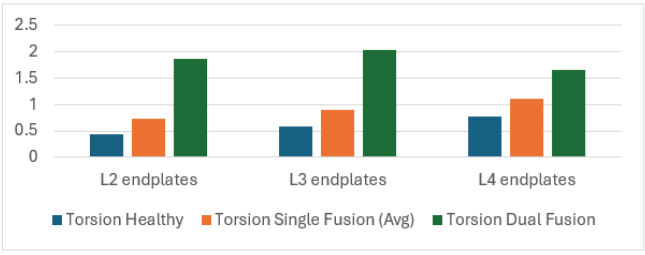


Figure 14c: Von Mises stress comparison at end plates for torsion.

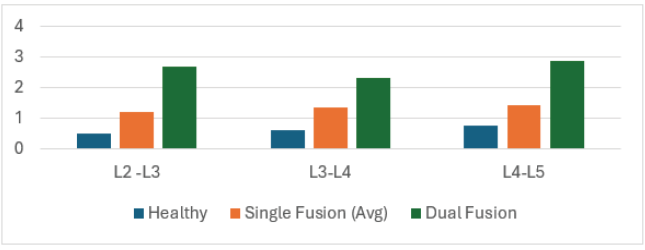


Figure 15a: Von Mises stress comparison at discs for flexion.

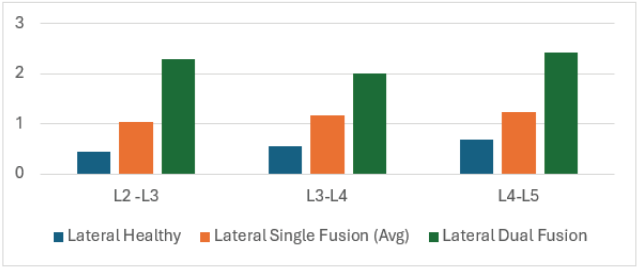


Figure 15b: Von Mises stress comparison at discs for lateral bending.

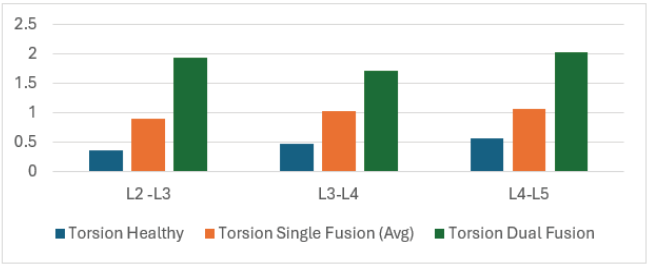


Figure 15c: Von Mises stress comparison at discs for torsion.

In the healthy lumbar configuration, endplate stress increased from the upper to the lower lumbar levels, serving as our reference for how load is transmitted throughout the spine. A prior study confirms that levels L4-L5 endplate stress is approximately 95% higher than L1-L2 under flexion-extension and lateral bending [60]. Stress magnitudes remained relatively low and evenly distributed between superior and inferior endplates at each level, indicating a balanced load across the vertebrae. Intervertebral disc von Mises stress also increased gradually toward L4-L5, with a relatively uniform distribution across the disc region, consistent with prior finite element analyses [60]. Also consistent with our findings, finite element studies, confirmed by in vivo data, have shown that increased trunk flexion elevates intradiscal pressure at L4-L5 [61]. Additionally, prior finite element analyses demonstrate elevated von Mises stress in the posterior annulus fibrosus and vertebral endplates during flexion-extension and lateral bending [60,62]. This baseline establishes that the lumbar spine, under normal conditions, distributes load predictably and progressively, and that deviations from this pattern following fusion indicate mechanical risk at the adjacent segment.

Single-level fusion altered the baseline stress. Adjacent endplates exhibited increased von Mises stress compared with the healthy model, with the magnitude depending on the fusion level. Fusions at the levels L3-L4 and L4-L5 produced larger stress elevations at neighboring endplates compared to more cranial fusions, which makes sense due to greater bending and load carried by the lower lumbar spine. Prior finite element analyses of an L4-L5 fusion of the spine have confirmed greater endplate stress in caudal endplates of the fusion level rather than the cranial end [63].

Disc stress in dual-level fusion models exhibited strong localization at the disc periphery with markedly higher stresses at the outer annulus compared to the healthy configuration (Figure 13). As the construct length increased, fewer motion segments remained available to share the redistributed load, resulting in sharper stress concentrations, particularly under lateral bending and torsion, where shear-driven mechanisms dominate (Table 7). Compared to single-level fusion, the increase in adjacent disc stress in dual-level fusion cases was substantially larger, underscoring the cumulative effect of multilevel constraint.

Compared to the healthy configuration, dual-level fusion resulted in an overall increase in adjacent level endplate and disc stress on the order of three to four times, depending on the loading mode. These findings reinforce the notion that construct length is a key surgical variable, one that determines the mechanical burden placed on unfused segments.

Discussion

Adjacent segment disease is one of the most common long-term complications of lumbar fusion, frequently requiring reoperation due to pain and functional decline [57]. While its clinical presentation is well-recognized, the underlying mechanical drivers have been difficult to study directly. Stress redistribution at adjacent endplates and discs cannot be measured intraoperatively or visualized on postoperative imaging. The ability to predict these changes computationally is important because elevated endplate and annular stresses have been associated with microfracture, disc herniation, and segmental failure [58]. Most finite element studies of lumbar fusion rely on homogeneous material assignment, which does not account for patient-specific variations in bone density and may misrepresent how load is actually transferred across vertebral endplates and intervertebral discs [59]. Without properly accounting for material properties, computational analyses may misrepresent stress transfer across vertebral endplates and intervertebral discs, leading to inaccurate predictions of ASD. By incorporating CT-based heterogeneous material properties, this study provides a more anatomically accurate simulation of stress redistribution by capturing the spatial variation in bone stiffness that influences where mechanical demand may concentrate following fusion.

Our findings reveal a clear and clinically relevant hierarchy: the healthy spine maintained balanced stress gradients across all lumbar levels; single-level fusion produced localized stress amplification at adjacent levels; and dual-level fusion resulted in even greater stress concentration at adjacent levels. Most importantly, this increase in stress was nonlinear; each additional fused level produced a disproportionate rise in adjacent segment stress, particularly under flexion and lateral bending, suggesting that construct length has compounding mechanical consequences that may not be fully appreciated in clinical decision-making.

In the single-level fusion, neighboring endplates experienced stress increases of approximately 1.3 to 1.7 times the healthy baseline, with greater amplification seen at lower lumbar levels under flexion and lateral bending, reflecting the higher mechanical load already carried by the caudal spine, and this stress magnitude also aligns with previous findings [64,65]. Implant material plays an important role, as cage stiffness has been shown to influence endplate stress distribution more than posterior rod material [66], suggesting that construct choice should account for implant properties as a variable in adjacent-segment risk. Intervertebral discs adjacent to single-level fusion levels also experienced elevated stress, consistent with prior finite element analyses reporting greater adjacent disc stress at L4-L5 compared with L3-L4 [65]. This is also accompanied by a shift in stress distribution toward the outer annulus, particularly during flexion [64,67]. Disc stress migration to the annulus is clinically significant because the annulus fibrosus is susceptible to damage and degeneration [68]. This redistribution is due to the constraint of the fused segment, which forces adjacent discs to accommodate higher bending moments and shear loads. This pattern of annular stress concentration mirrors the mechanical environment that precedes disc degeneration clinically, suggesting a possibility that ASD may be present immediately following fusion, and long before symptoms arise.

Dual-level fusion configurations produced the most pronounced stress amplification across both endplates and intervertebral discs. Endplate stress at adjacent unfused levels increased substantially compared to both healthy and single-level fusion models, reaching two to four times the healthy baseline depending on the fusion level and loading mode, with the greatest amplification observed at upper lumbar levels under flexion and lateral bending. This effect was particularly evident under flexion and lateral bending, where dual-level constraints reduced the number of vertebrae remaining to share the load and, as a result, mechanical demand was concentrated at fewer sites. This can elevate endplate stress to levels that exceed physiologic tolerance, leading to microdamage or subsidence. Intervertebral disc stress in dual-level fusion models showed marked localization at the outer annulus, indicating that a disproportionate load is concentrated at a degeneration-prone region of the disc.

Across configurations, increasing construct length was associated with a progressive and nonlinear shift in stress magnitude and localization; however, this increase was not linear, as the increase in stress from single- to dual-level fusion was substantially greater than that from the healthy to single-level condition (Figure 14). Prior finite element analyses have shown higher annulus fibrosus stress at adjacent segments following three-level lumbar fusion compared with two-level constructs [69], consistent with our observation of increased stress localization at the disc annulus with increasing construct length (Figure 15). An additional finite element study confirmed greater intradiscal pressure at adjacent segments with two-level fusion compared with single-level fusion, and model predictions were also validated through in vitro testing [65]. This nonlinearity is clinically important because surgeons cannot simply extrapolate the risk from a single-level fusion and double it to plan a two-level construct. Instead, the adjacent-segment burden scales faster than the construct does.

Limitations

Our study has a few limitations worth acknowledging. A formal mesh convergence study, with systematic revisions and comparisons of range of motion across element sizes, was not performed. The mesh was generated once, pre-assigned with material properties during CT-based segmentation, and used directly for analysis; however, the agreement between the initial model's range of motion output and cadaveric validation data (Figures 7-9) suggested that the mesh was adequate. Ideally, a formal mesh convergence study would be conducted to evaluate the ideal element size for stress outputs. Also, the peripheral localization trend reported in figures 12-13 reflects the regional average across the underlying node-levels rather than a uniform shift of every node to the outer annulus, and nodes near sharp reconstructed corners are incorporated into these averages, so this should be considered when interpreting these results. This study evaluated the L1-L3 and L3-L5 dual-level fusion constructs, but did not include the L2-L4 configuration. As a result, level-dependent trends are inferred from the most extreme two-level constructs rather than all possible combinations. Future work should include the L2-L4 construct to see whether stress amplification trends are continuous across fusion position. Additionally, ligaments and disc material properties are non-linear and hyperplastic, so it may be better to capture these elements from MRI. Loading was applied as pure moments and rotations at the superior endplate, which is standard for cadaveric validation protocol but does not account for muscle forces that are involved. Since physiologic loading in vivo includes axial compression from body weight and active muscle stabilization, the stress magnitudes reported here likely underestimate total loading at the endplates and discs, and future models should incorporate a follower load to approximate this. Also, facet joints were not modelled in this analysis. Since facet contact can contribute to load sharing, its exclusion could overestimate the stress transfer through the disc and endplates under these loading conditions. Our exploratory study used a single-patient model, so a cohort-based validation study would be necessary for generalizable clinical guidance.

Future Directions

This simulation captures lumbar spine behaviors by modelling these tissues as orthotropic structures using CT-

derived density mapping. Stress redistribution at adjacent discs and endplates are not visible on MRI and CT, yet it drives ASD. By quantifying these changes across healthy, single-, and dual-level fusion configurations, this study provides a mechanistic explanation for why multilevel fusion accelerates ASD despite achieving its primary goal of stabilization. These findings have direct implications for surgical planning and construct selection. Single-level fusion has a measurable but moderate mechanical cost to neighbouring segments. Dual-level fusion amplifies that cost three to four times, concentrated at the outer annulus where degeneration originates. Surgeons weighing single versus dual constructs should factor not only the immediate stability gained with fusion but also the cumulative mechanical burden placed on the unfused regions, particularly in patients with pre-existing risk factors such as osteoporosis, obesity, or advanced age, where the adjacent segment may be less equipped to tolerate elevated stress.

There are still significant gaps in our understanding of ASD prevention. Current clinical tools cannot identify which patients will develop symptomatic ASD before it occurs, and there is no consensus on how to select a fusion instrument that will minimize ASD risk. CT-based computational modelling can help address this gap by incorporating patient-specific bone density and geometry to generate predictions that reflect individual anatomy, rather than relying on population averages. Since we conducted a multi-modal analysis, these findings can be extended to patient-specific biomechanical questions, such as how occupational whole-body vibration (such as long haul driving) can impact lumbar loading, or assessing interbody cage durability. Our findings also complement prior patient-specific mechanoregulation studies that show fusion-induced alterations can cause changes in adjacent-disc composition and vertebral bone density. A study by Van Rijsbergen et al. showed agreement between computationally predicted tissue adaptation and clinical follow-up following fusion [127]. Our findings characterize an upstream component of this process, demonstrating that the magnitude and spatial distribution of adjacent-segment stress depends on the fusion length and location. Future work could couple the observed stress distributions with bone remodelling algorithms to evaluate whether construct-specific stress elevations translate into progressive changes in disc composition or vertebral bone density. As these models become more precise, they hold promise as preoperative planning tools for surgeons to simulate the mechanical consequences of their construct choice before surgery, identify vulnerable adjacent segments, and make more informed decisions about fusion extent, implant selection, and postoperative surveillance.

References

1. Woods KRM, Billys JB, Hynes RA. Technical description of oblique lateral interbody fusion at L1–L5 (OLIF25) and at L5–S1 (OLIF51), and evaluation of complications and fusion rates. The Spine Journal 17 (2017): 545-553.
2. Ohiorhenuan IE, Martirosyan NL, Wewel JT, et al. Lateral Interbody Fusion at L4/5: Management of the Transitional Psoas. World Neurosurgery 148 (2021): e192-e196.
3. Abel NA, Januszewski J, Vivas AC, Uribe JS. Femoral nerve and lumbar plexus injury after minimally invasive lateral retroperitoneal transpsoas approach: electrodiagnostic prognostic indicators and a roadmap to recovery. Neurosurg Rev 41 (2018): 457-464.
4. Pham MH, Hassan O, Diaz-Aguilar LD, Lehman RA. Complications Associated With Oblique Lumbar Interbody Fusion at L5-S1: A Systematic Review of the Literature. Neurosurg Open 2 (2021).
5. Shah M, Kolb B, Yilmaz E, et al. Comparison of Lumbar Laminectomy Alone, Lumbar Laminectomy and Fusion, Stand-alone Anterior Lumbar Interbody Fusion, and Stand-alone Lateral Lumbar Interbody Fusion for Treatment of Lumbar Spinal Stenosis: A Review of the Literature. Cureus 11 (2019): e5691.
6. Ozgur BM, Aryan HE, Pimenta L, Taylor WR. Extreme Lateral Interbody Fusion (XLIF): a novel surgical technique for anterior lumbar interbody fusion. Spine J 6 (2006): 435-443.
7. Agarwal N, White MD, Zhang X, et al. Impact of endplate-implant area mismatch on rates and grades of subsidence following stand-alone lateral lumbar interbody fusion: an analysis of 623 levels. J Neurosurg Spine 33 (2020): 12-16.
8. Malham GM, Ellis NJ, Parker RM, et al. Maintenance of Segmental Lordosis and Disk Height in Stand-alone and Instrumented Extreme Lateral Interbody Fusion (XLIF). Clin Spine Surg 30 (2017): E90-E98.
9. Watkins R, Hanna R. Non-union rate with stand-alone lateral lumbar interbody fusion. Medicine (Baltimore) 93 (2014): e275.
10. Winder MJ, Gambhir S. Comparison of ALIF vs. XLIF for L4/5 interbody fusion: pros, cons, and literature review. J Spine Surg 2 (2016): 2-8.
11. Bocahut N, Audureau E, Poignard A, et al. Incidence and impact of implant subsidence after stand-alone lateral lumbar interbody fusion. Orthop Traumatol Surg Res 104 (2018): 405-410.
12. O'Toole JE, Eichholz KM, Fessler RG. Surgical site infection rates after minimally invasive spinal surgery. J Neurosurg Spine 11 (2009): 471-476.
13. Li H, Li J, Tao Y, et al. Is stand-alone lateral lumbar interbody fusion superior to instrumented lateral lumbar

interbody fusion for the treatment of single-level, low-grade, lumbar spondylolisthesis? J Clin Neurosci 85 (2021) :84-91.

14. Marchi L, Abdala N, Oliveira L, et al. Stand-alone lateral interbody fusion for the treatment of low-grade degenerative spondylolisthesis. ScientificWorldJournal (2012): 456346.
15. Ahmadian A, Bach K, Bolinger B, et al. Stand-alone minimally invasive lateral lumbar interbody fusion: multicenter clinical outcomes. J Clin Neurosci 22 (2015): 740-746.
16. Screven R, Pressman E, Rao G, et al. The Safety and Efficacy of Stand-Alone Lateral Lumbar Interbody Fusion for Adjacent Segment Disease in a Cohort of 44 Patients. World Neurosurg 149 (2021): e225-e230.
17. Aichmair A, Alimi M, Hughes AP, et al. Single-Level Lateral Lumbar Interbody Fusion for the Treatment of Adjacent Segment Disease: A Retrospective Two-Center Study. Spine (Phila, Pa 1976) 42 (2017): E515-E522.
18. Katz AD, Singh H, Greenwood M, Cote M, Moss IL. Clinical and Radiographic Evaluation of Multilevel Lateral Lumbar Interbody Fusion in Adult Degenerative Scoliosis. Clin Spine Surg 32 (2019): E386-E396.
19. Ziino C, Konopka JA, Ajiboye RM, et al. Single position versus lateral-then-prone positioning for lateral interbody fusion and pedicle screw fixation. J Spine Surg 4 (2018): 717-724.
20. Patel RD, Graziano GP, Vanderhave KL, et al. Facet Violation With the Placement of Percutaneous Pedicle Screws: Spine. 2011; 36 (2011): E1749-E1752.
21. Mobbs RJ, Raley DA. Complications With K-Wire Insertion for Percutaneous Pedicle Screws. Journal of Spinal Disorders & Techniques 27 (2014): 390-394.
22. Zhao Q, Zhang H, Hao D, et al. Complications of percutaneous pedicle screw fixation in treating thoracolumbar and lumbar fractures. Medicine 97 (2018): e11560.
23. Hiyama A, Katoh H, Sakai D, et al. Accuracy of Percutaneous Pedicle Screw Placement after Single-Position versus Dual-Position Insertion for Lateral Interbody Fusion and Pedicle Screw Fixation Using Fluoroscopy. Asian Spine J 16 (2022): 20-27.
24. Pimenta L, Turner AWL, Dooley ZA, et al. Biomechanics of Lateral Interbody Spacers: Going Wider for Going Stiffer. The Scientific World Journal (2012): 1-6.
25. Manzur MK, Steinhaus ME, Virk SS, et al. Fusion rate for stand-alone lateral lumbar interbody fusion: a systematic review. Spine J. 2020;20(11):1816-1825.
26. Cappuccino A, Cornwall GB, Turner AWL, et al. Biomechanical analysis and review of lateral lumbar fusion constructs. Spine 35 (2010): S361-367.
27. Lang G, Navarro-Ramírez R, Gandevia L, et al. Elimination of Subsidence with 26-mm-Wide Cages in Extreme Lateral Interbody Fusion. World Neurosurg 104 (2017): 644-652.
28. Mok JM, Forsthoefel C, Diaz RL, Lin Y, Amirouche F. Biomechanical Comparison of Unilateral and Bilateral Pedicle Screw Fixation after Multilevel Lumbar Lateral Interbody Fusion. Global Spine Journal 14 (2024): 1524-1531.
29. Mok JM, Lin Y, Tafur JC, Diaz RL, Amirouche F. Biomechanical Comparison of Multilevel Stand-Alone Lumbar Lateral Interbody Fusion With Posterior Pedicle Screws: An In Vitro Study. Neurospine 20 (2023): 478-486.
30. Song C, Chang H, Zhang D, Zhang Y, Shi M, Meng X. Biomechanical Evaluation of Oblique Lumbar Interbody Fusion with Various Fixation Options: A Finite Element Analysis. Orthopedic Surgery 13 (2021): 517-529.
31. Cho JH, Hwang CJ, Kim H, et al. Effect of osteoporosis on the clinical and radiological outcomes following one-level posterior lumbar interbody fusion. Journal of Orthopaedic Science 23 (2018): 870-877.
32. Formby PM, Kang DG, Helgeson MD, Wagner SC. Clinical and Radiographic Outcomes of Transforaminal Lumbar Interbody Fusion in Patients with Osteoporosis. Global Spine Journal 6 (2016): 660-664.
33. Hou Y, Yuan W. Influences of disc degeneration and bone mineral density on the structural properties of lumbar end plates. The Spine Journal 12 (2012): 249-256.
34. Tawara D, Sakamoto J, Murakami H, et al. Mechanical evaluation by patient-specific finite element analyses demonstrates therapeutic effects for osteoporotic vertebrae. Journal of the Mechanical Behavior of Biomedical Materials 3 (2010): 31-40.
35. Zou D, Yue L, Fan Z, et al. Biomechanical Analysis of Lumbar Interbody Fusion Cages With Various Elastic Moduli in Osteoporotic and Non-osteoporotic Lumbar Spine: A Finite Element Analysis. Global Spine J 14 (2024): 2053-2061.
36. Wu J, Miao J, Chen G, et al. Finite element biomechanical analysis of 3D printed intervertebral fusion cage in osteoporotic population. BMC Musculoskelet Disord 25 (2024): 129.
37. Liu X, Ma J, Park P, et al. Biomechanical comparison of multilevel lateral interbody fusion with and without

supplementary instrumentation: a three-dimensional finite element study. BMC Musculoskelet Disord 18 (2017): 63.

38. Liang Z, Cui J, Zhang J, et al. Biomechanical evaluation of strategies for adjacent segment disease after lateral lumbar interbody fusion: Is the extension of pedicle screws necessary? BMC Musculoskelet Disord 21 (2020): 117.

39. Tao EX, Zhang RJ, Zhang B, et al. Biomechanical changes of oblique lumbar interbody fusion with different fixation techniques in degenerative spondylolisthesis lumbar spine: a finite element analysis. BMC Musculoskelet Disord 25 (2024): 664.

40. Han Z, Ren B, Zhang L, et al. Finite Element Analysis of a Novel Fusion Strategy in Minimally Invasive Transforaminal Lumbar Interbody Fusion. Biomed Res Int (2022): 4266564.

41. Zhang M, Ren W, Mo Z, et al. Biomechanics of adjacent segment after three-level lumbar fusion, hybrid single-level semi-rigid fixation with two-level lumbar fusion. Comput Methods Biomech Biomed Engin 25 (2022): 455-463.

42. Giambini H, Qin X, Dragomir-Daescu D, et al. Specimen-specific vertebral fracture modeling: a feasibility study using the extended finite element method. Med Biol Eng Comput 54 (2016): 583-593.

43. Cappetti N, Naddeo A, Naddeo F, Solitro GF. Finite elements/Taguchi method-based procedure for the identification of the geometrical parameters significantly affecting the biomechanical behavior of a lumbar disc. Computer Methods in Biomechanics and Biomedical Engineering 19 (2016): 1278-1285.

44. Schmidt H, Heuer F, Simon U, et al. Application of a new calibration method for a three-dimensional finite element model of a human lumbar annulus fibrosus. Clinical Biomechanics 21 (2006): 337-344.

45. Wiczenbach T, Pachocki L, Daszkiewicz K, et al. Development and validation of lumbar spine finite element model. PeerJ 11 (2023): e15805.

46. Qi W, Yan Y, Zhang Y, et al. Study of stress distribution in pedicle screws along a continuum of diameters: a three-dimensional finite element analysis. Orthopaedic Surgery 3 (2011):57-63.

47. Lu Y. Lateral lumbar interbody fusion: indications and techniques. In: Schmidek and Sweet: Operative Neurosurgical Techniques (2012): 1963-1972.

48. Zhang Z, Fogel GR, Liao Z, et al. Biomechanical analysis of lumbar interbody fusion cages with various lordotic angles: a finite element study. Computer Methods in Biomechanics and Biomedical Engineering 21 (2018): 247-254.

49. Goel VK, Ramirez SA, Kong W, Gilbertson LG. Cancellous Bone Young's Modulus Variation Within the Vertebral Body of a Ligamentous Lumbar Spine—Application of Bone Adaptive Remodeling Concepts. Journal of Biomechanical Engineering 117 (1995): 266-271.

50. Akamaru T, Kawahara N, Sakamoto J, et al. The Transmission of Stress to Grafted Bone Inside a Titanium Mesh Cage Used in Anterior Column Reconstruction After Total Spondylectomy: A Finite-Element Analysis: Spine 30 (2005): 2783-2787.

51. Zhao G, Wang L, Wang H, et al. Biomechanical Effects of Multi-segment Fixation on Lumbar Spine and Sacroiliac Joints: A Finite Element Analysis. Orthop Surg 16 (2024): 2499-2508.

52. Peng X, Li S, Yang S, et al. Biomechanical Characterization of Unilateral and Bilateral Posterior Lumbar Interbody Fusion Constructs. Li P, ed. BioMed Research International 1 (2022): 7081238.

53. Wu H, Shan Z, Zhao F, Cheung JPY. Poor Bone Quality, Multilevel Surgery, and Narrow and Tall Cages Are Associated with Intraoperative Endplate Injuries and Late-onset Cage Subsidence in Lateral Lumbar Interbody Fusion: A Systematic Review. Clin Orthop Relat Res 480 (2022): 163-188.

54. Singh V, Oppermann M, Evaniew N, et al. Lateral Lumbar Interbody Fusion With rhBMP-2 Can Achieve High Fusion Rates in Adult Spine Deformity Surgeries. Global Spine J 14 (2024): 244-256.

55. Vergari C, Gaume M, Persohn S, et al. From in vitro evaluation of a finite element model of the spine to in silico comparison of spine instrumentations. J Mech Behav Biomed Mater 123 (2021): 104797.

56. Zhang S, Zhang Y, Okuda L, et al. Oblique lateral interbody fusion with internal fixation in the treatment of cross-segment degenerative lumbar spine disease at L2 to L3 and L4 to L5: A finite element analysis. Journal of Orthopaedic Surgery and Research

57. Huang X, Cai Y, Chen K, et al. Risk factors and treatment strategies for adjacent segment disease following spinal fusion (Review). Mol Med Rep 31 (2024): 33.

58. Okuda S, Nagamoto Y, Matsumoto T, et al. Adjacent Segment Disease After Single Segment Posterior Lumbar Interbody Fusion for Degenerative Spondylolisthesis: Minimum 10 Years Follow-up. Spine (2018): E1384.

59. Chevalier Y, Pahr D, Zysset PK. The Role of Cortical Shell and Trabecular Fabric in Finite Element Analysis of the Human Vertebral Body. J Biomech Eng [Internet]. 2009 Oct 16 [cited 2026 Jan 8]; 131(111003).

60. Kang S, Park CH, Jung H, et al. Analysis of the physiological load on lumbar vertebrae in patients with osteoporosis: a finite-element study. Sci Rep 12 (2022): 11001.

61. Jo M, Chae SW. Stress analysis of intervertebral disc during occupational activities. Comput Methods Programs Biomed 208 (2021): 106298.

62. Ahmadi M, Zhang X, Lin M, et al. Automated Finite Element Modeling of the Lumbar Spine: A Biomechanical and Clinical Approach to Spinal Load Distribution and Stress Analysis. World Neurosurg. 201 (2025): 124236.

63. Umale S, Yoganandan N, Baisden JL, et al. A biomechanical investigation of lumbar interbody fusion techniques. J Mech Behav Biomed Mater 125 (2022): 104961.

64. Pradeep K, Pal B. Effects of open and minimally invasive Transforaminal Lumbar Interbody Fusion (TLIF) surgical techniques on mechanical behavior of fused L3-L4 FSU: A comparative finite element study. Med Eng Phys 123 (2024): 104084.

65. Azadi A, Arjmand N. A comprehensive approach for the validation of lumbar spine finite element models investigating post-fusion adjacent segment effects. J Biomech 121 (2021): 110430.

66. Wang H, Wan Y, Liu X, et al. The biomechanical effects of Ti versus PEEK used in the PLIF surgery on lumbar spine: a finite element analysis. Comput Methods Biomech Biomed Engin 24 (2021): 1115–1124.

67. Ebrahimkhani M, Arjmand N, Shirazi-Adl A. Adjacent segments biomechanics following lumbar fusion surgery: a musculoskeletal finite element model study. Eur Spine J 31 (2022): 1630-1639.

68. Tsantrizos A, Ito K, Aebi M, Steffen T. Internal Strains in Healthy and Degenerated Lumbar Intervertebral Discs. Spine 30 (2005): 2129.

69. Zhang M, Ren W, Mo Z, et al. Biomechanics of adjacent segment after three-level lumbar fusion, hybrid single-level semi-rigid fixation with two-level lumbar fusion. Comput Methods Biomech Biomed Engin 25 (2022): 455-463.

70. Potter BK, Freedman BA, Verwiebe EG, et al. Transforaminal Lumbar Interbody Fusion: Clinical and Radiographic Results and Complications in 100 Consecutive Patients. Clin Spine Surg 18 (2005):337.

71. Resnick DK, Choudhri TF, Dailey AT, et al. Guidelines for the performance of fusion procedures for degenerative disease of the lumbar spine. Part 7: intractable low-back pain without stenosis or spondylolisthesis. J Neurosurg Spine 2 (2005): 670-672.

72. Fourney DR, Abi-Said D, Rhines LD, et al. Simultaneous anterior—posterior approach to the thoracic and lumbar spine for the radical resection of tumors followed by reconstruction and stabilization. J Neurosurg Spine 94 (2001): 232-244.

73. Parisini P, Di Silvestre M, Greggi T, et al. Surgical Correction of Dystrophic Spinal Curves in Neurofibromatosis: A Review of 56 Patients. Spine 24 (1999): 2247.

74. Dhillon K. Spinal Fusion for Chronic Low Back Pain: A 'Magic Bullet' or Wishful Thinking? Malays Orthop J 10 (2016): 61-68.

75. Chen WJ, Lai PL, Niu CC, et al. Surgical Treatment of Adjacent Instability After Lumbar Spine Fusion. Spine 26 (2001): E519.

76. Cao L, Liu Y, Mei W, et al. Biomechanical changes of degenerated adjacent segment and intact lumbar spine after lumbosacral topping-off surgery: a three-dimensional finite element analysis. BMC Musculoskelet Disord 21 (2020): 104.

77. Ebrahimkhani M, Arjmand N, Shirazi-Adl A. Biomechanical effects of lumbar fusion surgery on adjacent segments using musculoskeletal models of the intact, degenerated and fused spine. Sci Rep 11 (2021): 17892.

78. Adams MA, Roughley PJ. What is Intervertebral Disc Degeneration, and What Causes It? Spine 31 (2006): 2151.

79. Sato K, Kikuchi S, Yonezawa T. In Vivo Intradiscal Pressure Measurement in Healthy Individuals and in Patients With Ongoing Back Problems. Spine 24 (1999): 2468.

80. Oxland TR. Fundamental biomechanics of the spine—What we have learned in the past 25 years and future directions. J Biomech 49 (2016): 817-832.

81. Ferguson SJ, Steffen T. Biomechanics of the aging spine. Eur Spine J 12 (2003): S97-103.

82. Pye SR, Reid DM, Lunt M, et al. Lumbar disc degeneration: association between osteophytes, end-plate sclerosis and disc space narrowing. Ann Rheum Dis 66 (2007): 330-333.

83. Jin H, Luo J, Jiang Y, et al. Osteophyte formation causes neurological symptoms after anterior cervical discectomy and fusion (ACDF): A case report. Front Surg 9 (2023): 1029743.

84. Gerling MC, Leven D, Passias PG, et al. Risk Factors for Reoperation in Patients Treated Surgically for Lumbar Stenosis: A Subanalysis of the 8-year Data From the SPORT Trial. Spine 41 (2016): 901.

85. Radcliff K, Curry P, Hilibrand A, et al. Risk for Adjacent Segment and Same Segment Reoperation After Surgery for Lumbar Stenosis: A Subgroup Analysis of the Spine Patient Outcomes Research Trial (SPORT). Spine 38 (2013): 531.

86. Bashkuev M, Reitmaier S, Schmidt H. Effect of disc degeneration on the mechanical behavior of the human lumbar spine: a probabilistic finite element study. Spine J 18 (2018): 1910-1920.

87. Hilibrand AS, Robbins M. Adjacent segment degeneration and adjacent segment disease: the consequences of spinal fusion? Spine J. 2004 Nov 1;4(6, Supplement): S190-194.

88. Phillips FM, Carlson GD, Bohlman HH, Hughes SS. Results of Surgery for Spinal Stenosis Adjacent to Previous Lumbar Fusion. Clin Spine Surg 13 (2000): 432.

89. Etebar S, Cahill DW. Risk factors for adjacent-segment failure following lumbar fixation with rigid instrumentation for degenerative instability. J Neurosurg Spine 90 (1999): 163-169.

90. Aiki H, Ohwada O, Kobayashi H, et al. Adjacent segment stenosis after lumbar fusion requiring second operation. J Orthop Sci 10 (2005): 490-495.

91. Tobert DG, Antoci V, Patel SP, et al. Adjacent Segment Disease in the Cervical and Lumbar Spine. Clin Spine Surg 30 (2017): 94.

92. Hashimoto K, Aizawa T, Kanno H, Itoi E. Adjacent segment degeneration after fusion spinal surgery—a systematic review. Int Orthop 43 (2019): 987-993.

93. Ou CY, Lee TC, Lee TH, Huang YH. Impact of Body Mass Index on Adjacent Segment Disease After Lumbar Fusion for Degenerative Spine Disease. Neurosurgery 76 (2015): 396.

94. Stokes IAF, Iatridis JC. Mechanical Conditions That Accelerate Intervertebral Disc Degeneration: Overload Versus Immobilization. Spine 29 (2004): 2724-2732.

95. Rothenfluh DA, Mueller DA, Rothenfluh E, Min K. Pelvic incidence-lumbar lordosis mismatch predisposes to adjacent segment disease after lumbar spinal fusion. Eur Spine J 24 (2015): 1251-1258.

96. Sears WR, Sergides IG, Kazemi N, et al. Incidence and prevalence of surgery at segments adjacent to a previous posterior lumbar arthrodesis. Spine J 11 (2011): 11-20.

97. Lu K, Liliang PC, Wang HK, et al. Reduction in adjacent-segment degeneration after multilevel posterior lumbar interbody fusion with proximal DIAM implantation. J Neurosurg Spine 23 (2015): 190-196.

98. Harrop JS, Youssef JA, Maltenfort M, et al. Lumbar Adjacent Segment Degeneration and Disease After Arthrodesis and Total Disc Arthroplasty. Spine 33 (2008): 1701.

99. Anakwenze OA, Auerbach JD, Milby AH, et al. Sagittal Cervical Alignment After Cervical Disc Arthroplasty and Anterior Cervical Discectomy and Fusion: Results of a Prospective, Randomized, Controlled Trial. Spine 34 (2009): 2001.

100. Kelly MP, Mok JM, Frisch RF, Tay BK. Adjacent Segment Motion After Anterior Cervical Discectomy and Fusion Versus ProDisc-C Cervical Total Disk Arthroplasty: Analysis from a Randomized, Controlled Trial. Spine 36 (2011): 1171.

101. Ramírez-Villaescusa J, López-Torres Hidalgo J, Ruiz-Picazo D, Martín-Benlloch A. A descriptive study on the adjacent segment degeneration related signs following a lumbar fusion procedure. J Spine Surg 7 (2021): 354–63.

102. He C, Wan Y, Wang Y, et al. Imaging analysis of adjacent segment disease combined with retrolisthesis after posterior lumbar interbody fusion: a preliminary cross-sectional comparative study. Quant Imaging Med Surg 15 (2025): 111811191–111811191.

103. Zhou L, Qiao Y, Cai Q, et al. Global trends and insights in ethical statements regarding the utilization of human cadaveric tissues for biomechanical research from 2017 to 2022: a bibliometric analysis. Int J Surg Lond Engl 111 (2024): 1503-1507.

104. Cartner JL, Hartsell ZM, Ricci WM, Tornetta P. Can We Trust Ex Vivo Mechanical Testing of Fresh–Frozen Cadaveric Specimens? The Effect of Postfreezing Delays. J Orthop Trauma 25 (2011): 459-461.

105. Jiang S, Li W. Biomechanical study of proximal adjacent segment degeneration after posterior lumbar interbody fusion and fixation: a finite element analysis. J Orthop Surg 14 (2019): 135.

106. Park WM, Choi DK, Kim K, et al. Biomechanical effects of fusion levels on the risk of proximal junctional failure and kyphosis in lumbar spinal fusion surgery. Clin Biomech 30 (2015): 1162-1169.

107. Naoum S, Vasiliadis AV, Koutserimpas C, et al. Finite Element Method for the Evaluation of the Human Spine: A Literature Overview. J Funct Biomater 12 (2021): 43.

108. Lu T, Lu Y. Comparison of Biomechanical Performance Among Posterolateral Fusion and Transforaminal, Extreme, and Oblique Lumbar Interbody Fusion: A Finite Element Analysis. World Neurosurg 129 (2019): e890-9.

109. Xu H, Ju W, Xu N, et al. Biomechanical Comparison of

Transforaminal Lumbar Interbody Fusion With 1 or 2 Cages by Finite-Element Analysis. Oper Neurosurg 73 (2013): ons198.

110. Wang Y, Shen Q, Liang C, et al. Biomechanical Analysis of Adjacent Segments after Spinal Fusion Surgery Using a Geometrically Parametric Patient-Specific Finite Element Model. J Vis Exp JoVE 203 (2024): e66247.

111. Azadi A, Arjmand N. A comprehensive approach for the validation of lumbar spine finite element models investigating post-fusion adjacent segment effects. J Biomech 121 (2021): 110430.

112. Ruberté LM, Natarajan RN, Andersson GBJ. Influence of single-level lumbar degenerative disc disease on the behavior of the adjacent segments—A finite element model study. J Biomech 42 (2009): 341-348.

113. Ebrahimkhani M, Arjmand N, Shirazi-Adl A. Adjacent segments biomechanics following lumbar fusion surgery: a musculoskeletal finite element model study. Eur Spine J 31 (2022): 1630-1639.

114. Zhang M, Ren W, Mo Z, et al. Biomechanics of adjacent segment after three-level lumbar fusion, hybrid single-level semi-rigid fixation with two-level lumbar fusion. Comput Methods Biomech Biomed Engin 25 (2022): 455-463.

115. Antonacci CL, Zeng F, Jackson C, et al. Lateral interbody fusion for adjacent segment disease: a narrative review. J Spine Surg 10 (2024): 286-294.

116. Rabau O, Navarro-Ramirez R, Aziz M, et al. Lateral Lumbar Interbody Fusion (LLIF): An Update. Glob Spine J 10 (2020): 17S-21S.

117. Lee HJ, Lee SJ, Jung J myung, et al. Biomechanical Evaluation of Lateral Lumbar Interbody Fusion with Various Fixation Options for Adjacent Segment Degeneration: A Finite Element Analysis. World Neurosurg 173 (2023): e156–67.

118. Shimooki Y, Murakami H, Nishida N, et al. Finite Element Modeling for Biomechanical Comparisons of Multilevel Transforaminal, Posterior, and Lateral Lumbar Approaches to Interbody Fusion Augmented with Posterior Instrumentation. World Neurosurg 182 (2024): e463–70.

119. Nikkhoo M, Chen WC, Lu ML, et al. Anatomical parameters alter the biomechanical responses of adjacent segments following lumbar fusion surgery: Personalized poroelastic finite element modeling investigations. Front Bioeng Biotechnol [Internet]. 2023 Feb 13 [cited 2025 Dec 1];11. Available from: https://www.frontiersin.org/journals/bioengineering-and-biotechnology/articles/10.3389/fbioe.2023.1110752/full

120. Soltani Z, Xu M, Radovitzky R, et al. CT-based finite element simulating spatial bone damage accumulation predicts metastatic human vertebrae strength and stiffness. Front Bioeng Biotechnol 12 (2024): 1424553.

121. Dall'Ara E, Pahr D, Varga P, et al. QCT-based finite element models predict human vertebral strength in vitro significantly better than simulated DEXA. Osteoporos Int 23 (2012): 563-572.

122. Kim KJ, Kim DH, Lee JI, et al. Hounsfield Units on Lumbar Computed Tomography for Predicting Regional Bone Mineral Density. Open Med 14 (2019): 545-551.

123. Irmola, Tero Matti MD∗; Häkkinen, Arja Prof†, ‡; Järvenpää, et al. Reoperation Rates Following Instrumented Lumbar Spine Fusion. SPINE 43 (2018): p295-301.

124. Xia XP, Chen HL, Cheng HB. Prevalence of adjacent segment degeneration after spine surgery: a systematic review and meta-analysis. Spine (Phila Pa 1976), 38 (2013): 597-608.

125. Kumar MN, Baklanov A, Chopin D. Correlation between sagittal plane changes and adjacent segment degeneration following lumbar spine fusion. Eur Spine J 10 (2001): 314-319.

126. Tobias Pitzen, Fred Geisler, Dieter Matthis, et al. A finite element model for predicting the biomechanical behaviour of the human lumbar spine. Control Engineering Practice. 10 (2002).

127. van Rijsbergen M, van Rietbergen B, Barthelemy V, et al. Comparison of patient-specific computational models vs. clinical follow-up, for adjacent segment disc degeneration and bone remodelling after spinal fusion. PLoS One 13 (2018): e0200899.

This article is an open access article distributed under the terms and conditions of the Creative Commons Attribution (CC-BY) license 4.0

Citation: Amirouche F, Kurup S, Rajavel H. Predicting postoperative spinal load redistribution following single- and dual-level lumbar fusion: an in-silico analysis. Journal of Spine Research and Surgery. 8 (2026): 82-100.